Proceedings of Montreal 2018
Global Power and Propulsion Forum
7th - 9th May, 2018
www.gpps.global

GPPS-NA-2018-0008

LARGE EDDY SIMULATION OF A ROTOR STAGE FOR FAN NOISE SOURCE DIAGNOSTIC

Carlos Pérez Arroyo, Marlene Sanjose, Stéphane Moreau
Université de Sherbrooke
Carlos.Perez.Arroyo@USherbrooke.ca
Sherbrooke, Quebec, Canada

Florent Duchaine
CERFACS
Florent.Duchaine@cerfacs.fr
Toulouse, France

Abstract

A Large Eddy Simulation (LES) of the NASA Source Diagnostic Test turbofan is performed focusing on a single rotor blade without the stator vanes to put emphasis on the grid resolution in both the tip clearance and the rotor wake without any potential effect from the stator. The investigated operating condition is representative of approach conditions for which the rotor is operating out-of-design. Good agreement with aerodynamic measurements is observed at two different axial positions for the mean and wake turbulence values. In the LES, the boundary layer naturally transitions to turbulence on the blade suction side but remains quasi laminar over most of its pressure side. Flow visualizations capture the tip leakage flow and the complex influence of resolved coherent structures in the boundary layer and wake development. Last, the Power Spectral Density is analyzed in the wake and on the blades for the axial velocity and pressure fluctuations respectively.

Introduction

Turbofan architecture has evolved toward an increasing contribution of the fan to the thrust and consequently to the overall engine noise. Indeed, at approach conditions the fan noise has become one of the main contributors with a main broadband content mostly in the forward arc of the engine. This will be all the more for future turbo-engines that will involve Ultra-High By-pass Ratio (UHBR) turbofans. For these architectures, fan noise is projected to become the dominant source overall. In a classical turbofan as the present configuration, the interaction between the wake of the rotor and equally-distributed Outlet-Guide Vanes (OGV) has been found to be the dominant mechanism that contributes to fan noise (Ruijgrok, 2004; Peake and Parry, 2012). On the one hand, tonal noise can be more easily controlled by clever choice of blade counts (Tyler and Sofrin, 1962) and taking advantage of the duct filtering to have the first Blade Passing Frequency (BPF) cut-off for instance. On the other hand, broadband noise has a significant contribution much harder to control especially at high frequencies given the high number of cut-on modes for modern engines with low hub-to-tip ratio. Yet, with increasing noise regulations for commercial aircrafts, it becomes mandatory to get a better understanding of the noise generation and propagation for fan and OGV interaction broadband noise in order to be able to properly guide further noise reduction technology development.

Progress in High Performance Computing (HPC) has allowed for the correct prediction of complex flows around isolated parts of turbomachines with Reynolds Averaged Navier-Stokes (RANS), unsteady RANS, Large Eddy Simulations (LES) and high-fidelity Direct Numerical Simulations (DNS) (Tucker, 2011). However, only the latter two methods (LES and DNS) can provide the multi-scale noise sources that yield broadband noise. A recent review (Gourdain et al., 2014) gives an overview of LES industrial compressor flows and reports simulations with full stages highlighting the cost of LES for multistage compressors (de Laborderie et al., 2013; Gourdain, 2015). But all these simulations involved low-pressure com-

This work is licensed under a
Creative Commons Attribution-NonCommercial-NoDerivatives 4.0 International License CC-BY-NC-ND 4.0

pressor with small blade spans, reduced rotor-stator distances and moderate Reynolds numbers based on the chord.

The "Fan Noise Source Diagnostic Test" (SDT) experimental set-up was investigated by NASA to provide an extensive database of aerodynamic sources and aeroacoustic diagnostics of the broadband fan/OGV interaction mechanism (Hughes et al., 2002; Podboy, Krupar, Helland and Hughes, 2002; Woodward et al., 2002). This study is the continuation of previous works (Leonard et al., 2016; Pérez Arroyo et al., 2017) where the full configuration (including rotor blades, stator vanes and the nacelle), was computed with LES in an azimuthally periodic domain of $2\pi/11$. From this simulation, Leonard *et al.* computed the wake turbulent statistics from the LES results used in an analytical model to predict the rotor-stator interaction noise. Pérez Arroyo *et al.* focused on instantaneous aerodynamic features and the comparison of two acoustic analogies for noise propagation. In the present work, a new LES is performed on a reduced domain consisting on one single blade, without any stator vanes in order to focus the computational cost on an accurate description of the wake and the tip-gap vortices responsible of low-frequency noise. The latter mechanism was significantly under-predicted in previous simulations, and was thought to be the origin of some spurious low-frequency humps in the far-field noise predictions.

The NASA experiment is summarized in the next section. The complete numerical model and parameters are then provided. Finally both steady and unsteady (noise sources) aerodynamic results from the LES are shown.

Experimental set-up

As part of the NASA advanced Subsonic Technology Noise Reduction Program, several experiments (Hughes et al., 2002; Woodward et al., 2002; Envia, 2002; Podboy, Krupar, Helland and Hughes, 2002; Podboy, Krupar, Hughes and Woodward, 2002) have been carried out on the Source Diagnostic Test rig presented involving different geometries and counts of the rotor blades and stator outlet vanes. The configuration studied here is the baseline configuration designed by General Electric Aircraft Engines which is composed of 22 rotor blades (R4) and 54 radial stator vanes.This $1/5$th scale model fan stage is representative of the secondary stream of a modern High Bypass-Ratio turbofan engine. Note that the experimental set-up does not involve a core flow.

The approach condition has the most extensive experimental data set and is investigated in the present numerical study. Free-stream Mach number of 0.10 is imposed, to achieve acoustic flight effects and to provide far-field acoustic data representative of actual approach conditions (Woodward et al., 2002). The rotational speed is 7808 rpm corresponding to 61.7% of the rotor design speed. The overall test program had many phases, including detailed flow field diagnostic measurements using laser Doppler and hot-wire anemometry (Podboy, Krupar, Helland and Hughes, 2002; Podboy, Krupar, Hughes and Woodward, 2002) and acoustic power measurements (Woodward et al., 2002) including configurations with only the rotor stage (Hughes et al., 2002).

Numerical parameters

Computational Domain

Following previous studies (Leonard et al., 2016; Pérez Arroyo et al., 2017) (hereafter quoted as LES-RS), only a periodic portion of the fan stage is simulated. Moreover, the domain is further simplified by only simulating one rotor blade without any stator vanes. This simplification removes any possibility to properly capture azimuthal modes or instabilities but allows to decrease the computational costs of the simulation while increasing the mesh resolution in the wake and close to the casing in order to resolve the wake with a finer mesh for a reduced cost. In addition, not modeling the stator vanes removes its potential effect on the rotor wake development, with possibly some non-linear coupling (Sanjosé et al., 2017). As shown in Fig. 1, the domain extends in the axial direction about three rotor-chords before the rotor leading edge (LE), and about one rotor-chord after the theoretical position of the stator trailing edge (TE). This allows to perform the simulation with only one moving reference frame simplifying the wake extractions on the theoretical stator leading edge plane used in several acoustic analytical models. The current simulation is referenced as LES-RO.

Unstructured Mesh

The unstructured mesh used in the present LES simulation is shown along a blade-to-blade view at mid-channel height in Fig. 2. The mesh has 68.7 million cells or equivalently 12.7 million nodes. The cell size in the rotor wake is progressively increased until reaching the outlet boundary condition with a mesh size of 1.8 mm. Upstream of the rotor blades the mesh is uniform and coarsen up to a mesh size of 1.5 mm at the inlet. The spatial discretization around the blades has 8 layers of prisms for a good discretization of the near-wall region where the majority of cells have a y^+ of about 15. Overall, the mesh

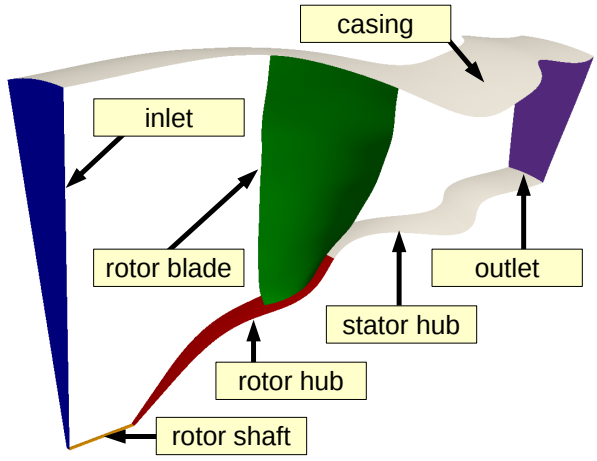

Figure 1 View of the computational domain.

is more refined than in previous works with cells located outside the wakes, half the original size. Furthermore, in order to focus on an accurate resolution of the tip-gap vortices and the rotor wake, a higher refinement in these regions is applied. Nevertheless, the tip-gap region is discretized with 8 layers of prisms and an average of 7 tetrahedral elements to reach the casing as in the LES-RS case. The minimum cell size in the tip-gap has been kept constant with respect to the mesh used in LES-RS to avoid an increase of the total cost of the simulation as a smaller cell size would considerably impact the time-step of the simulation.

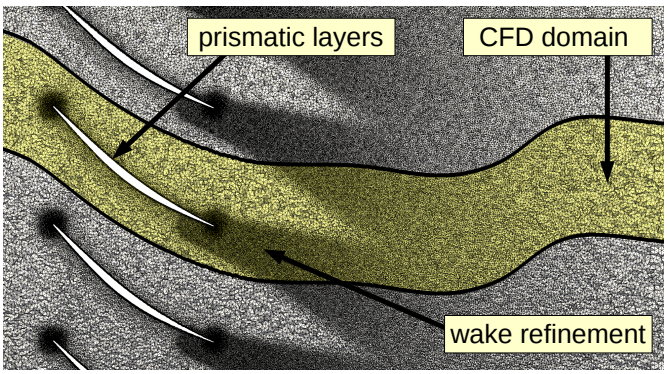

Figure 2 Grid in a blade-to-blade cut at mid-channel height.

Large Eddy Simulation

The AVBP code developed by CERFACS and IFPEN (Schönfeld and Rudgyard, 1999) has been used for the compressible LES. The numerical scheme for the present LES is an explicit Lax-Wendroff second order scheme both in space and time. The time step for the simulation has been set to approximately 1.2×10^{-5} ms to have $29,000$ iterations per blade passage keeping the local CFL number based on the characteristics below 0.7. The sub-grid scale model used is the Wall-Adapting Local Eddy-viscosity model (WALE) that provides the proper turbulence decay toward the walls. As for the turbine cases (Papadogiannis et al., 2016), a log-law model (which switches to a linear model for $y^+ < 11.445$) is applied on all walls.

The inlet and outlet conditions are based on characteristics (ingoing and exiting waves) and defined with a relaxation factor towards the mean variables of the full configuration LES-RS, i.e. velocity and temperature at the inlet and pressure at the outlet. The outlet condition takes into account transverse terms in the expression of the incoming wave amplitude to substantially reduce spurious acoustic wave reflections (Granet et al., 2010). The boundary condition at the shaft is defined as wall slip whereas all other wall boundary conditions are defined with no slip and a log-law model. While the rotor hub and the blade walls are rotating with the domain, the boundary condition for the stator hub defines a counter-rotating wall in the ALE methodology. Moreover, periodic conditions are set on the lateral sides of the domain.

The simulation is initialized from the mean solution from LES-RS and after a transient regime of about 4 rotation times, statistics have been extracted from the simulation during 4 rotations (about 28 ms).

Aerodynamic Results

Mean Flow

In Tab. 1 mass-flow rate and total pressure ratio computed from both simulations are compared showing differences of less than 3% with respect to experiments (Hughes et al., 2002). Overall, good agreement is obtained with experiments despite the major differences such as: domain size, boundary conditions, frames of references and of course, the elimination of the stator vanes in the new simulation. Nonetheless, variations between 6 and 7% are found for the mean axial velocity. One of the reasons for such differences could be the fact that the simulated tip clearance corresponds to the sideline "hot" geometry with maximum loading that does not account for the same blade deformation in rotation.

Iso-contours of averaged Mach numbers are presented on blade-to-blade surfaces at three channel heights in Fig. 3. Flow is moving from left to right. The mean flow described by both simulations is very similar at midspan and near the hub. Nev-

	Mass-flow rate (kg/s)	**Total pressure ratio**	**Mean axial speed**(m/s)	
			Section 1	Section 2
Experiments(Hughes et al., 2002)	26.44	1.159	112.42	114.98
LES-RS	25.77 (-2.52%)	1.162 (+0.25%)	105.40 (-6.24%)	107.06 (-6.88%)
LES-RO	26.72 (+1.05%)	1.171 (+1.04%)	105.65 (-6.02%)	107.43 (-6.56%)

Table 1 Performances for the baseline configuration at 61.7% rotor speed and mean axial velocity V_{ref} at mid-distance between the rotor and the stator (Section 1) and at the stator leading edge plane (Section 2).

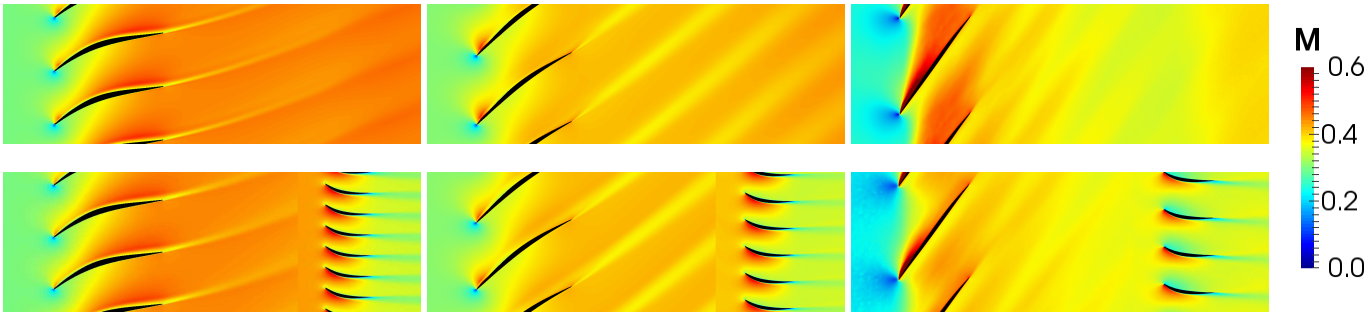

Figure 3 Averaged Mach number contours on developed blade-to-blade surfaces for the LES-RO (top) and LES-RS (bottom). Left: 25% channel height. Center: 50% channel height. Right: 97% channel height.

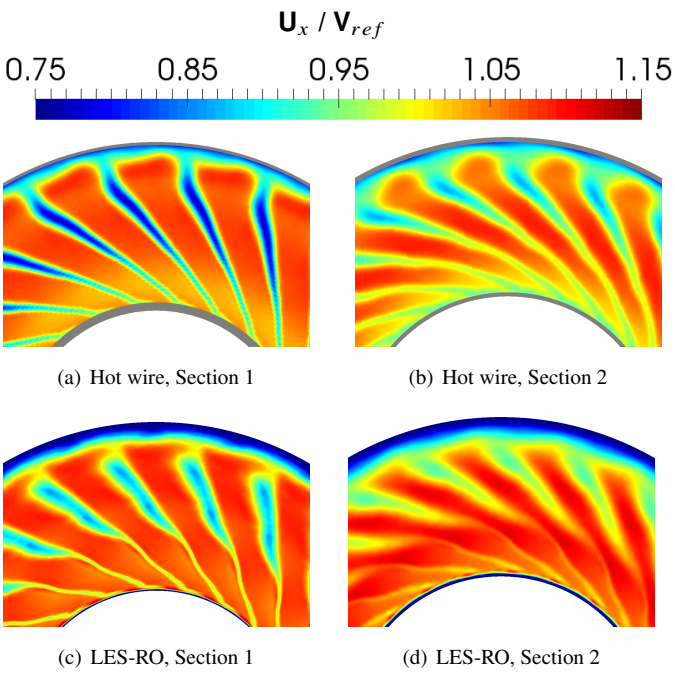

(a) Hot wire, Section 1 (b) Hot wire, Section 2

(c) LES-RO, Section 1 (d) LES-RO, Section 2

Figure 4 Normalized mean axial velocity flow fields.

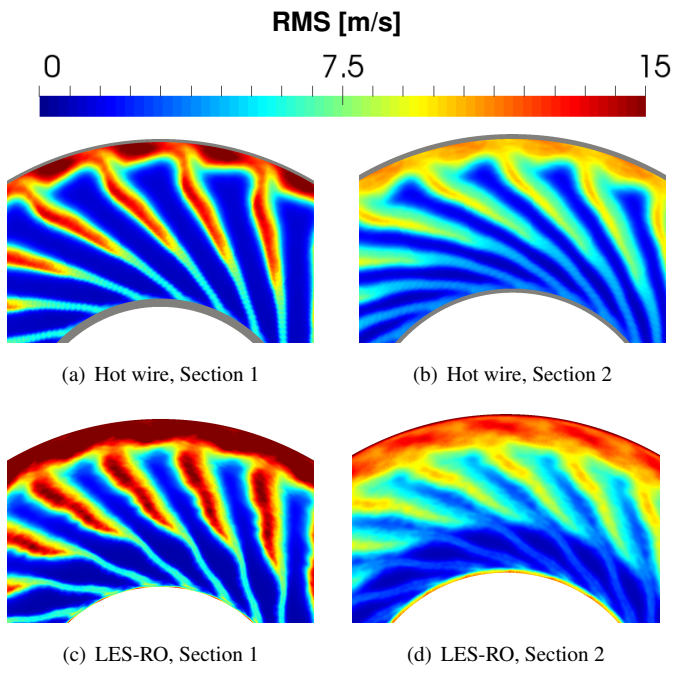

(a) Hot wire, Section 1 (b) Hot wire, Section 2

(c) LES-RO, Section 1 (d) LES-RO, Section 2

Figure 5 RMS of axial velocity flow fields.

ertheless, the wakes are thinner and less dissipated in the LES-RO simulation near the hub (25% of span) due to the higher refinement of the wake region. At mid-span, a higher intensity is shown in the rotor leading edge for LES-RO. At the tip (97% of span) the LES-RO mesh has been redesigned with smaller cells on the surface of the casing and on the rotor leading edge. This allows for a better discretization of the tip-gap flow which shows a higher Mach number through the whole channel.

Figure 4 presents the field of the normalized component of axial velocity in axial cuts at mid-distance between the rotor trailing edge and the stator leading edge plane (Section 1) and at the stator leading edge reference plane (Section 2) where

hot-wire (HW) measurements have been performed (Podboy, Krupar, Hughes and Woodward, 2002). The values are normalized by the respective (experimental, or LES) mean axial velocity at the axial plane of interest in order to take into account deviations from the experimental operational point given in Tab. 1. In Section 1, the twisting effect on the rotor wake caused by the differential transport of the wake vorticity by the mean swirl is well captured by LES-RO as it was found in the LES-RS case. Similarly, the top 10% of the channel is strongly affected by the tip leakage flow resulting in a flow blockage and a strong axial velocity deficit. This is hardly seen in the HW measurements, which may still suggest an insufficient mesh resolution in the tip clearance. Finally the LES-RO normalized axial velocity outside the wake agrees well with experiments, even though the wake deficit is slightly underpredicted. Close to the hub, LES-RO shows a finer wake as shown in Fig. 3. In Section 2, further away from the rotor, similar results are found near the tip with a higher deficit in axial velocity. The shape of the wake is in good agreement with the experimental results even though the levels are in average higher near to the hub which may be attributed to different operating conditions caused by the fact that experiments were run with the skewed stator stage.

The unsteady nature of the LES also allows obtaining statistics of the resolved turbulent velocity fluctuations: the RMS of the axial velocity are presented in Fig. 5 along with experimental results. The turbulence pattern obtained by LES, for both the wakes and the tip secondary flow, shows a good agreement with the experiments in Section 1. Moreover in the wake, they have similar levels in most of the channel height. In Section 2, the wake shows similar levels and shapes in the regions away from the casing. Near the tip-gap region, the RMS values are higher and cover a larger region than in experiments.

Note that similar flow behavior has been reported (Casalino et al., 2018) using a hybrid Lattice-Boltzmann/Very Large Eddy Simulation (LBM/VLES) model of the baseline SDT configuration. Yet, in this hybrid model a tripping device needed to be introduced close to the blade leading edge over the whole span to trigger transition to turbulence and yield the proper turbulent levels in the wake. No tip gap caused by the voxel resolution could be captured in the coarsest simulations.

Unsteady Flow and Noise Sources

One advantage of LES is to give access to detailed information on the turbulence development that can help to understand its influence on the noise sources of the turbofan operating at approach condition. The turbulent structures are identified using an iso-surface of Q-criterion computed using velocity components on a fixed reference frame. Q stands for the second invariant of the velocity-gradient tensor. The iso-surface at $Q = 1 \times 10^7\ \mathrm{s}^{-2}$ is shown in Fig. 6 on the pressure and suction sides of the blade.

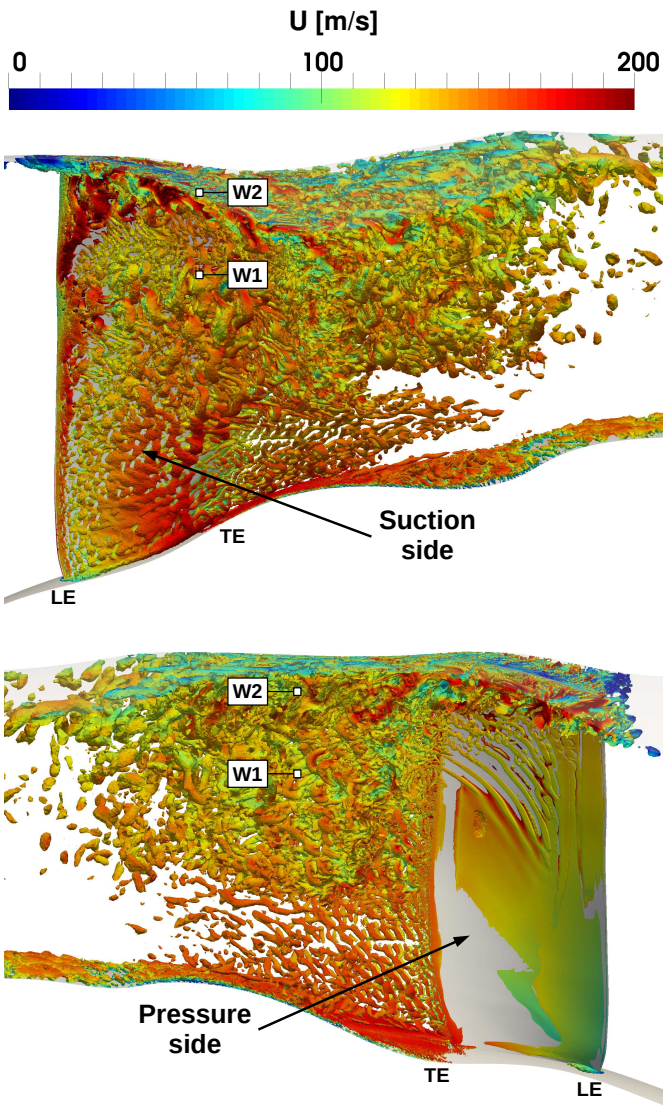

Figure 6 Q-criterion iso-surfaces colored by velocity magnitude and reference probes locations W1 and W2 in the wake.

On the suction side, while the boundary layer is generally turbulent starting from the leading edge, two clear structures are visible, one develops at the leading edge between 50 and 75% of the channel height and it is convected downstream and another grows from 75% of the channel height to the tip. The latter structure rolls up and is convected towards the pressure side of the blade. The favorable pressure gradient on the pressure side limits the development of the turbulence (quasi laminar along the whole blade span): the boundary layer is initially

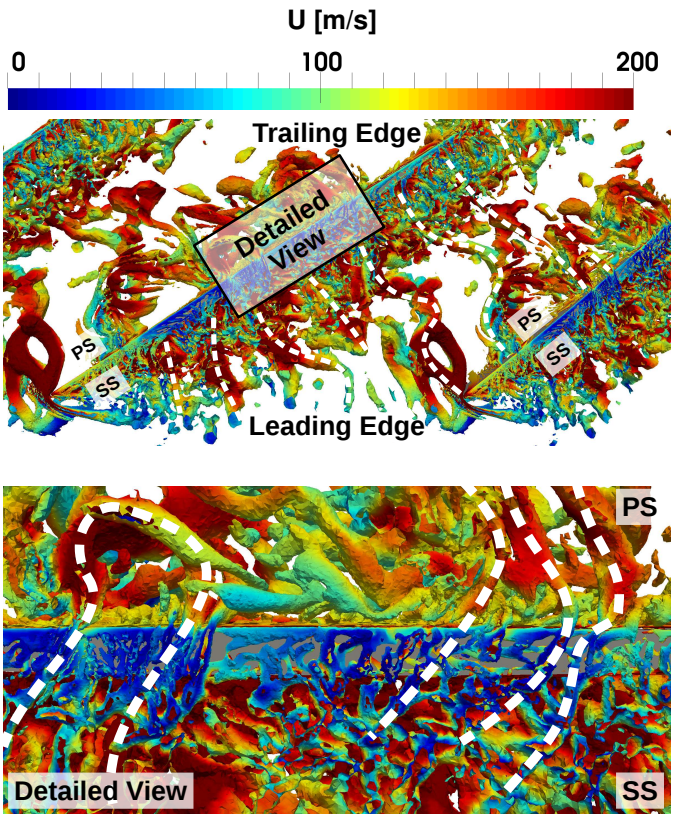

Figure 7 Q-criterion iso-surfaces above 95% of the span colored by velocity magnitude. (Bottom) Detailed view depicted in (top) by the black rectangle. Dashed lines depict the vortical structures captured by Q-criterion iso-surfaces. SS: Suction side. PS: Pressure side.

laminar and some turbulent spots can be localized by the appearance of vertical vortical structures on the upper part of the blade near the trailing edge. On 50% of the blade span close to the hub, no turbulent structures are visible revealing that the boundary layer seen as a vortex sheet stays in a quasi laminar state. This yields a very thin wake and low velocity deficit in the lower part of the channel as seen in Fig. 4 for both experimental and numerical results. Close to the tip, the structures that are developed on the suction side impact the blade on the pressure side trying to leak through the tip-gap to the suction side.

Indeed, a different view of the Q-criterion from the top of the blade clearly illustrates the above-mentioned phenomena. Figure 7 shows the Q-criterion above 95% of the span with $Q = 25 \times 10^7$ s^{-2}. The structures highlighted by the dashed lines are generated at the leading edge of the blade and are convected through the blade passage perpendicular to the blades until it reaches the leading edge of the following blade. In fact, part of these structures (shown in the detailed view) connect with the suction side energizing it.

Moreover, the vortical structures shown with the Q-criterion leave a trace on the blade skin wall pressure as shown in Fig. 8. From the RMS of pressure, both structures developing on the suction side are visible and are separated by a region without relevant pressure fluctuations between 70 and 80% of the channel height. The impact of the coherent structures on the leading edge tip are shown on the pressure side RMS along with the boundary layer development above 60% of the channel height.

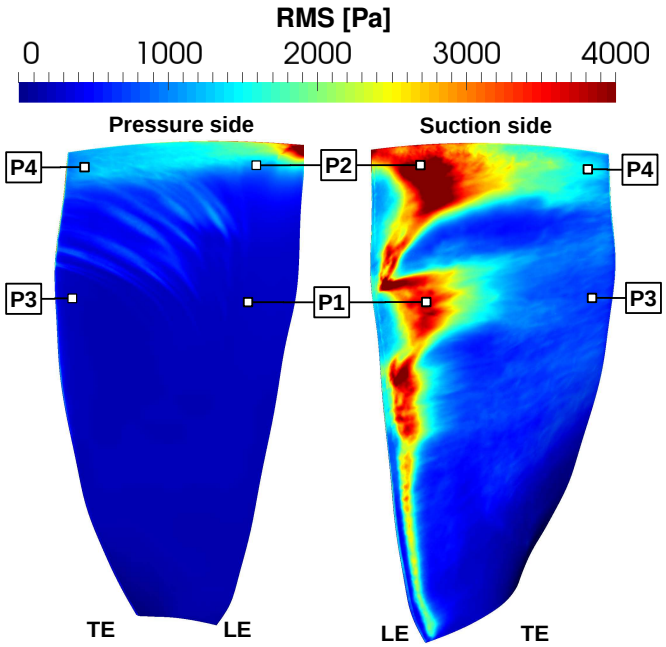

Figure 8 RMS of wall pressure fields on the rotor blade and location of pressure probes P1, P2, P3 and P4 on the blade surface.

Figure 9 shows the Power Spectral Density (PSD) computed for the axial velocity in the wake in the rotor frame of reference at points W1 and W2 depicted in Fig. 6 located at 75 and 97% of channel height respectively, and at about one chord of the trailing edge. These results are compared against the ones obtained for the LES-RS case. Both simulations give similar values of PSD for all the resolved frequency range at both locations. A finer mesh for LES-RO allows for a longer inertial subrange with slope of -5/3. At frequencies over 10 kHz, both locations give similar PSD levels and decay rates. On the other hand, at low frequencies the major differences appear. The location W2 situated near the casing, receives the impact of the vortices generated by the blade tip shown in Fig. 6 which can be decomposed in the ones developing on the suction side and the vortices rolling up on the pressure side that will in fact

contribute to the ones on the suction side by the tip leakage.

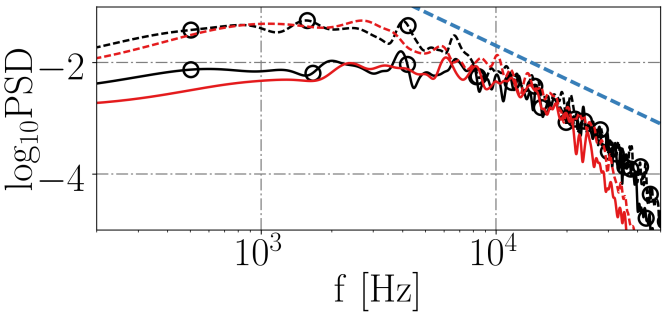

Figure 9 PSD of axial velocity in the wake at W1 and W2. LES-RO W1, LES-RO W2. LES-RS W1, LES-RS W2. $f^{-5/3}$.

In order to distinguish between both vortical structures as a first approach, the wall pressure PSD is computed on both sides of the blade at 4 different locations highlighted in Fig. 8. These locations have been selected on the suction side as characteristic locations where the vortical structures are shown to develop (P1 and P2 at $X/C = 0.2$) and where they are fully developed (P3 and P4 at $X/C = 0.9$). On the suction side, all results give a broadband spectrum without any relevant peaks. Both P1 and P2 show the same PSD levels for frequencies lower than 10 kHz. Over this frequency, the location P2 closer to the tip shows a richer spectrum that follows the -5 slope which indicates that it has a higher turbulent content. Near the trailing edge, P4 shows higher PSD levels with respect to the location P3. Moreover, P4 depicts a larger region with a -1 slope characteristic of pressure sources in the inertial range than P3. On the pressure side, the laminar boundary layer is well illustrated with the PSD at P1 and P3 several orders of magnitude lower than at P2 and P4. In addition, P2 and P4 receives the contribution of the vortical structures shed by the previous blade increasing its PSD amplitude. Last, the decay at higher frequencies is more abrupt than the one found in a turbulent boundary layer.

Conclusions and perspectives

The Large Eddy Simulation of the scale-model simplified NASA SDT turbofan rotor stage has been successfully achieved at approach conditions. This simulation was performed on a simplified domain of one single blade and no stator vanes in order to focus on the wake and tip-gap vortices development. LES results show a good overall agreement with experiments on the mean aerodynamic flow properties and the turbulent velocity fluctuations with hot-wire measurements. Noticeably, the bottom part of the wake is essentially lami-

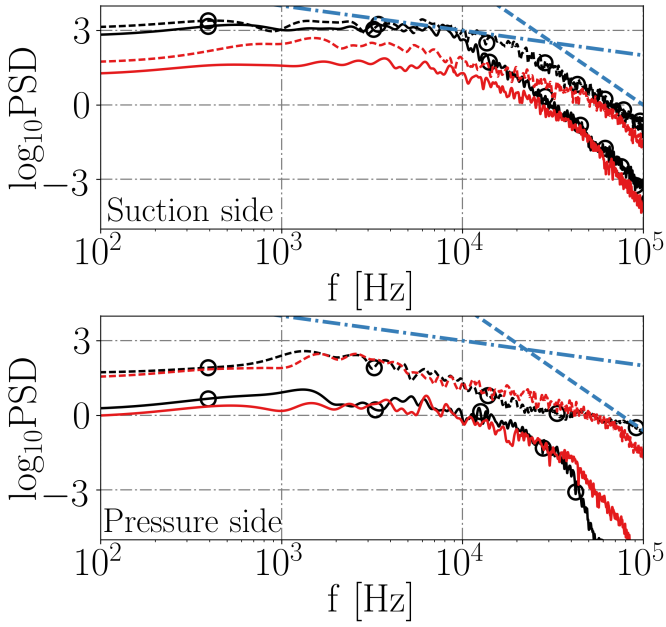

Figure 10 PSD of wall pressure on the blade at P1, P2, P3 and P4. P1, P2, P3, P4. f^{-1}, f^{-5}.

nar and much thinner than in previous works due to the higher refinement. The Q-criterion is computed at several snapshots which allows to show the formation of two coherent structures on the blade and different interactions. These structures leave a clear pattern on the wall pressure RMS on the blades. On the suction side, a coherent structure is generated from the leading edge at 70% of the span, these vortices roll up and eventually merge in the wake with the second vortical structure. The latter is also generated at the leading edge but closer to the tip-gap with a higher energy content on the low frequencies as shown by the wall pressure PSD. This structure not only grows with the boundary layer along the chord but is also shed on the tip and impacts the next blade pressure side which will then generate more fluctuations as shown in all pressure PSD results. Moreover, due to the tip-gap, these structures interact with the suction side along the whole chord. This study highlights the need of a better understanding of tip-gap flows for aeronautical turbomachinery with small tip-gaps, high rotating speeds and thin blades.

In future works, the effect of grid refinement in the gap should be further studied as well as the use of higher order schemes and different wall models on the blade and the casing. Moreover, far-field noise will be computed with acoustic analogies or analytical models and compared with measured spectra on the rotor alone.

Acknowledgments

This research was enabled in part by the computational resources provided by Mammoth-MP2 from Calcul Québec and Graham from Sharcnet managed by Compute Canada (www.computecanada.ca). The authors would like to thank E. Envia from NASA for providing the experimental data in the framework of the AIAA benchmark. The authors are grateful to CERFACS, which develops and provides us with AVBP for academic research.

References

Casalino, D., Hazir, A. and Mann, A. (2018), 'Turbofan broadband noise prediction using the Lattice Boltzmann Method', *AIAA Journal* **56**(2), 609–628.

de Laborderie, J., Moreau, S. and Berry, A. (2013), Compressor Stage Broadband Noise Prediction using a Large-Eddy Simulation and Comparisons with a Cascade Response Model, *in* '19th AIAA/CEAS Aeroacoustics Conference, Berlin, Germany', AIAA-2013-2042.

Envia, E. (2002), Fan Noise Source Diagnostics Test - Vane Unsteady Pressure Results, *in* '8th AIAA/CEAS Aeroacoustics Conference & Exhibit, Breckenridge, Colorado', AIAA-2002-2430.

Gourdain, N. (2015), 'Prediction of the unsteady turbulent flow in an axial compressor stage. Part 1: Comparison of unsteady rans and les with experiments', *Computers & Fluids* **106**, 119–129.

Gourdain, N., Sicot, F., Duchaine, F. and Gicquel, L. (2014), 'Large eddy simulation of flows in industrial compressors: a path from 2015 to 2035', *Phil. Trans. R. Soc. A* **372**(2022), 20130323.

Granet, V., Vermore, O., LÃl'onard, T., Gicquel, L. and Poinsot, T. (2010), 'Comparison of Nonreflecting Outlet Boundary Conditions for Compressible Solvers on Unstructured Grids', *AIAA Journal* **48**(10), 2348–2364.

Hughes, C., Jeracki, R., Woodward, R. and Miller, C. (2002), Fan Noise Source Diagnostic Test - Rotor Alone Aerodynamic Performance Results, *in* '8th AIAA/CEAS Aeroacoustics Conference & Exhibit, Breckenridge, Colorado', AIAA-2002-2426.

Leonard, T., Sanjosé, M., Moreau, S. and Duchaine, F. (2016), Large Eddy Simulation of a scale-model turbofan for fan noise source diagnostic, *in* '22nd AIAA/CEAS Aeroacoustics Conference, Lyon, France', AIAA-2016-3000.

Papadogiannis, D., Duchaine, F., Gicquel, L., Wang, G. and Moreau, S. (2016), 'Effects of Subgrid Scale Modeling on the Deterministic and Stochastic Turbulent Energetic Distribution in Large-Eddy Simulations of a High-Pressure Turbine Stage', *Journal of Turbomachinery* **138**(9), 091005–091005.

Peake, N. and Parry, A. B. (2012), 'Modern challenges facing turbomachinery aeroacoustics', *Annual Review of Fluid Mechanics* **44**, 227–248.

Pérez Arroyo, C., Leonard, T., Sanjose, M., Moreau, S. and Duchaine, F. (2017), Large Eddy Simulation of a Scale-model Turbofan for Fan Noise Source Diagnostic, *in* 'ISROMAC 2017, Symposium on Rotating Machinery, Maui, HI, U.S.A.', Isromac.

Podboy, G., Krupar, M., Helland, S. and Hughes, C. (2002), Steady and Unsteady Flow Field Measurements within a NASA 22 inch fan model, *in* '40th AIAA Aerospace Sciences Meeting & Exhibit, Reno, NV, U.S.A.', AIAA-2002-1033.

Podboy, G., Krupar, M., Hughes, C. and Woodward, R. (2002), Fan Noise Source Diagnostic Test - LDV Measured Flow Field Results, *in* '8th AIAA/CEAS Aeroacoustics Conference & Exhibit, Breckenridge, Colorado', AIAA-2002-2431.

Ruijgrok, G. J. J. (2004), *Elements of Aviation Acoustics*, Delft University Press.

Sanjosé, M., Moreau, S., Pestana, M. and Roger, M. (2017), 'Effect of Weak Outlet-Guide-Vane Heterogeneity on Rotor–Stator Tonal Noise', *AIAA Journal* **55**(10), 3440–3457.

Schönfeld, T. and Rudgyard, M. (1999), 'Steady and Unsteady Flow Simulations Using the Hybrid Flow Solver AVBP', *AIAA Journal* **37**(11), 1378–1385.

Tucker, P. G. (2011), 'Computation of unsteady turbomachinery flows: Part 2 - LES and hybrids', *Progress in Aerospace Sciences* **47**(7), 546–569.

Tyler, J. M. and Sofrin, T. G. (1962), Axial flow compressor noise studies, Technical report, SAE Technical Paper.

Woodward, R., Hughes, C., Jeracki, R. and Miller, C. (2002), Fan Noise Source Diagnostic Test - Far-field Acoustic Results, *in* '8th AIAA/CEAS Aeroacoustics Conference & Exhibit, Breckenridge, Colorado', AIAA-2002-2427.